Available online at www.sciencedirect.com
ScienceDirect
Trans. Nonferrous Met. Soc. China 33(2023) 1755−1767
Transactions of Nonferrous Metals Society of China
www.tnmsc.cn

Development and characterizations of graded porous titanium scaffolds via selective laser melting for orthopedics applications

Ai-hua YU[1], Wei XU[1,2], Xin LU[1,2,3], Maryam TAMADDON[4], Bo-wen LIU[1], Shi-wei TIAN[5], Ce ZHANG[1], Muhammad Arif MUGHAL[6], Jia-zhen ZHANG[1], Chao-zong LIU[4]

1. National Engineering Research Center for Advanced Rolling and Intelligent Manufacturing, Institute of Engineering Technology, University of Science and Technology Beijing, Beijing 100083, China;
2. Shunde Innovation School, University of Science and Technology Beijing, Foshan 528399, China;
3. Beijing Advanced Innovation Center for Materials Genome Engineering, State Key Laboratory for Advanced Metals and Materials, University of Science and Technology Beijing, Beijing 100083, China;
4. Institute of Orthopaedic & Musculoskeletal Science, University College London, Royal National Orthopaedic Hospital, Stanmore HA7 4LP, UK;
5. National Engineering Technology Research Center of Flat Rolling Equipment, Institute of Engineering Technology, University of Science and Technology Beijing, Beijing 100083, China;
6. Institute of Artificial Intelligence, University of Science and Technology Beijing, Beijing 100083, China

Received 16 December 2021; accepted 24 May 2022

Abstract: To improve the treatment effect of bone defect repair, titanium scaffolds having graded structures with porosities of 78.8%, 70.8%, 62.6%, and 54.4% (denoted as P1, P2, P3, and P4, respectively) were designed and fabricated by selective laser melting. The manufacturability, microstructure, mechanical properties, and permeability were investigated theoretically and experimentally. Simulation results showed that the maximum von Mises stress and permeability were in the range of 569.1−1469.0 MPa and (21.7−54.6)×10^{-9} m^2 respectively. Thereinto, P3 and P4 exhibited lower maximum von Mises stress, meaning a higher strength. The microstructure of fabricated scaffolds with P3 and P4 consisted of martensitic α' phase. The yield strength and elastic modulus were 185.3−250.8 MPa and 6.1−9.7 GPa, respectively. Compared with the scaffold with P3, the scaffold with P4 exhibited higher yield strength and a more matched elastic modulus to cortical bone, and its permeability (18.6×10^{-9} m^2) was within the range of permeability of human bone. Comprehensively, the scaffold with P4 is a promising candidate for bone defect reconstructions.
Key words: graded porous titanium; bone implants; selective laser melting; mechanical properties; permeability

1 Introduction

Number of patients with bone defects caused by trauma or disease is increasing annually, and clinical results indicate that bone replacement is an effective method to treat bone defects. At present, orthopaedic implants usually are fabricated by using metal, ceramic and polymer materials, among which metal materials have significant advantages in fatigue resistance, and machinability. Among the metal materials, titanium (Ti) and its alloys, which have high specific strength, low elastic modulus, and excellent biocompatibility, have been widely used [1−3]. However, there are still a series of disadvantages with extensively used Ti−6Al−4V (Ti64) and commercially pure Ti (CP-Ti). For instance, both of them have higher elastic moduli

Corresponding author: Xin LU, Tel: +86-10-62332598-6678, E-mail: luxin@ustb.edu.cn;
Wei XU, Tel: +86-10-62332598-6832, E-mail: weixu@ustb.edu.cn
DOI: 10.1016/S1003-6326(23)66219-3

(Ti64 ~120 GPa, CP-Ti ~110 GPa) compared to natural bones (3−30 GPa for cortical bone) [4−6]. The mismatch of elastic modulus between implants and natural bones leads to the stress shielding effect, which causes peripheral bone resorption and ultimately the failure of implantation [7]. To overcome this problem, porous structure was introduced to the Ti matrix [8,9]. The porous structure not only reduces the elastic modulus significantly by adjusting porosity [10−13], but also improves the permeability of implants, which is beneficial for cell adhesion, proliferation and differentiation [14−16]. However, the strength of porous scaffolds inevitably decreases with the increase in porosity, which then raises the risk of fracture failure after implantation. Thus, there is an urgent demand to develop porous scaffolds with high strength and porosity for clinical applications.

For enhanced therapeutic effectiveness, graded porous scaffolds, mimicking the natural bones both morphologically and mechanically, have been developed recently [17−21]. In the past, fabricating a biomimetic graded scaffold via traditional manufacturing methods, for instance, slurry foaming, gas foaming, and investment casting, was a serious challenge due to the lack of accurate control over the shape, size, and distribution of pores [22]. But today, with the development of additive manufacturing (AM) technology, such as selective laser melting (SLM), electron beam melting (EBM), and selective laser sintering (SLS), the limitations of conventional manufacturing methods in fabricating implants with complex structures have been addressed [8,23,24]. In several additive manufacturing (AM) technologies, SLM is regarded as the most promising technology for fabricating graded porous structures due to its high precision [24,25].

Until now, lots of graded Ti-based alloy scaffolds have been manufactured by SLM and the properties were investigated [17,26−30]. For instance, CHOY et al [26] fabricated graded Ti64 scaffolds with cubic cells by SLM, and the mechanical test results showed that the yield strength of the graded porous sample was 67% higher than that of the uniform sample. WU et al [27] designed graded orthogonal structures and manufactured scaffolds by SLM. The results of compressive tests revealed that the yield strength of graded Ti64 specimens was greatly higher than that of single-porosity specimens at the same average porosity. However, the mechanical properties and permeability of bone scaffolds should match with the human bones to guarantee excellent mechanical and biological adaptability simultaneously. Previous studies mainly focused on investigating the mechanical properties of graded scaffolds, nonetheless, the permeability has been rarely studied. Hence, it is imperative to investigate the permeability and mechanical properties at the same time when designing the graded porous scaffolds with excellent mechanical and biological properties.

In the present work, four graded structures with different porosities were designed. The mechanical properties and permeability were investigated using finite element analysis (FEA) firstly. According to simulation results, CP-Ti scaffolds with optimized structures were fabricated by SLM, and the manufacturability, microstructure, compressive properties, as well as permeability were investigated systematically. It aims at designing the graded scaffolds and optimizing the mechanical properties to match the human natural bones, to provide basic guidance for its potential application in treating bone defects.

2 Experimental

2.1 Design and manufacturing of graded structures

Four graded structures that are based on unit cells with the characteristics of both edge-centered cubic and face-centered cubic, were constructed through SolidWorks software. The length of unit cells was 2 mm, while the different radii of struts (0.15−0.4 mm) were chosen. The overall dimensions of cubic specimens were 10 mm × 10 mm × 10 mm (length × width × height), and the average porosities were 78.8%, 70.8%, 62.6% and 54.4% (denoted as P1, P2, P3 and P4, respectively). The graded structures with decreasing porosity from the center to the perimeter, along the direction perpendicular to the building direction, were composed of three layers (i.e., Layers 1, 2 and 3, an example of P3 is shown in Fig. 1). The geometric parameters of designed unit cells and graded structures are listed in Table 1 and Table 2, respectively.

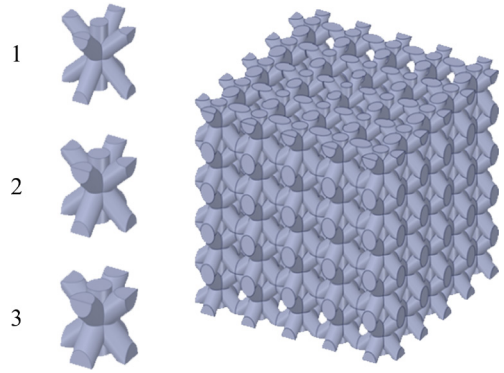

Fig. 1 Unit cells used by Layers 1, 2 and 3, and graded lattice structure of P3

Table 1 Geometric parameters of designed unit cells

Unit cell	Unit length/μm	Porosity/%	Strut radius/μm
1	2000	90.1	150
2	2000	83.3	200
3	2000	75.8	250
4	2000	67.6	300
5	2000	59.2	350
6	2000	51.1	400

Table 2 Geometric parameters of designed graded structures

Model	Layer	Unit cell	Average porosity/%
P1	1	1	78.8
	2	2	
	3	3	
P2	1	2	70.8
	2	3	
	3	4	
P3	1	3	62.6
	2	4	
	3	5	
P4	1	4	54.4
	2	5	
	3	6	

Hydride−dehydride titanium powder (HDH-Ti), provided by Beijing Xing Rong Yuan Co., Ltd., China, was selected as the raw material. In order to improve the flowability, the powder was ball-milled using a planetary ball-milling machine. The detailed process parameters of ball-milling treatment were described in our previous studies [31,32]. After ball-milling treatment, the powders were sieved by using an oscillating sieving machine to obtain the powders with a particle size of 23−45 μm for the SLM process.

The tested samples were fabricated by an SLM 125HL machine (SLM Solutions GmbH, Lübeck, Germany). The detailed parameters used during fabrication were as follows: laser power 150 W, scanning speed 385 mm/s, layer thickness 30 μm, and hatching space 0.12 mm. The hatching type of a continuous laser mode, in which the alternate angle is 33° between each layer, was chosen. And the graded scaffolds were built along the *Z*-axis direction that is perpendicular to the direction of the gradient. To minimize oxidation, the whole process was conducted under an argon gas atmosphere.

2.2 Finite element analysis (FEA)

The mechanical properties of designed graded structures were studied by FEA via Ansys Workbench, and the finite element model is displayed in Fig. 2(a). The material of graded structures in the middle was set as Ti, whose density, elastic modulus, Poisson ratio, and compressive yield strength are 4.51 g/cm^3, 110 GPa, 0.3, and 830 MPa, respectively [33]. The bottom plate was defined as fixed support, and the top rigid plate was loaded with a compressive force of

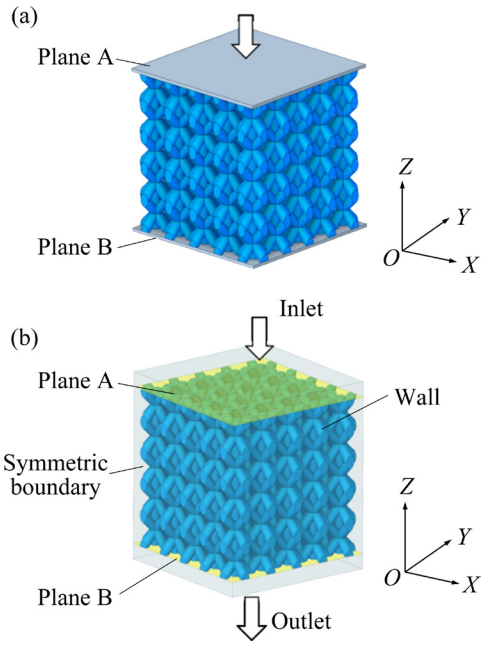

Fig. 2 Finite element analysis model and boundary conditions: (a) Mechanical analysis; (b) CFD analysis

4500 N (about 4.5 times the patient's mass which is assumed to be 100 kg) [34]. General contact with a friction coefficient of 0.1 was set between the contact surfaces of rigid plates and the designed graded structures during the loading process. The quadratic tetrahedral element (C3D10) was adopted to mesh the graded structures.

2.3 Computational fluid dynamics (CFD) analysis of permeability

Permeability of the graded structures was simulated by the module of Fluent of Ansys Workbench and the analysed models were identified as an incompressible fluid. The Navier-Stokes equation (Eqs. (1) and (2)) was used in this work, which is suitable for fully developed flow of an incompressible fluid with constant viscosity and density [35]:

$$\rho\frac{\partial v}{\partial t}-(v\cdot\nabla)v+\frac{1}{\rho}\nabla P-\mu\nabla^2 v=F \tag{1}$$

$$\nabla\cdot v=0 \tag{2}$$

where ρ is the fluid density, kg/m^3; v is the velocity, m/s; t is the time, s; μ is the dynamic viscosity coefficient of fluid, Pa·s; ∇ is the Del operator; P is the pressure, Pa; F is the force such as gravity and centrifugal force, and is set to 0.

The water was selected as a liquid for CFD analysis in this work. The simulated permeability of designed graded structures was calculated by [16]

$$k=\frac{v\mu L}{\Delta P} \tag{3}$$

where k is the permeability coefficient, m^2; v is the fluid velocity, m/s, and is selected as 0.001 m/s; μ is the dynamic viscosity coefficient of fluid, Pa·s, which is 10^{-3} Pa·s; L is the height of the models, m, which is 0.01 m; ΔP is the pressure difference between the top and its bottom, Pa. The CFD analysis model and boundary conditions are shown in Fig. 2(b), and the fluid area above the graded structures was used to avoid boundary effects. The greyish side faces were set as the symmetric boundary, and the blue surface was assumed to be a no-slip wall. Moreover, the inlet velocity was 0.001 m/s, and the pressure of the outlet was assumed as 0 Pa.

2.4 Characterization

The manufactured specimens were removed from the Ti baseplate by wire cutting, and then were sand-blasted and ultrasonically cleaned in absolute ethyl alcohol for 30 min to remove the powders attached to the surfaces of struts and entrapped in the pores. Following that, the samples were dried under a vacuum. The morphology of the graded structures was observed by scanning electron microscopy (SEM, JSM−6480LV). The phase of the scaffolds was identified using an X-ray diffractometer (Cu K_α, λ=0.15406 nm, Dmax-RB) at 50 kV and 200 mA with a diffraction angle from 30° to 80° and a scanning rate of 5 (°)/min. For the microstructure analysis, scanning electron microscopy (SEM, JSM−6480LV) and transmission electron microscopy (TEM, tecani G2 F20) were used.

The porosity of graded scaffolds was measured by the dry weighing method and Micro-CT (Phoenix v|tome|x, GE) at voltage of 70 kV and current of 100 μA, and the porosity was calculated by Eq. (4) in the dry weighting method. Each sample was measured five times repeatedly to get reliable results. The theoretical bulk density of CP-Ti was assumed to be 4.51 g/cm^3. The pore size was measured by Micro-CT.

$$p=\left(1-\frac{m_\mathrm{p}}{m_\mathrm{d}}\right)\times 100\% \tag{4}$$

where p is the porosity of the specimen; m_p is the mass of graded scaffolds, g; m_d is the mass of a solid cube with the same size as graded scaffolds, g.

Uniaxial compressive tests were conducted along the building direction (Z-axis) at room temperature via the universal testing machine (CMT4305), and the compressive strain rate of 0.01 mm/s was selected according to the ISO 13314:2011(E) [36]. In order to ensure the accuracy of results, three samples of each graded scaffold were measured.

The falling head method was used to evaluate the permeability of graded scaffolds, and Fig. 3 shows the experimental facility. The permeability of graded scaffolds can be calculated by Eq. (5) [37].

$$k=\frac{aH}{A(t_2-t_1)}\ln\frac{L_1\mu_0}{L_2\rho_0 g} \tag{5}$$

where a is the cross-section area of the standpipe, m^2; A is the cross-section area of the tested sample, m^2; H is the height of the sample, m; L_1 is the initial

height, m; L_2 is the final height, m; t_1 is the initial time at the height of L_1, s; t_2 is the final time at the height of L_2, s; μ_0 is the dynamic viscosity coefficient of water, which is 1×10^{-3} Pa·s; ρ_0 is the density of water; g is the acceleration of gravity, m/s^2.

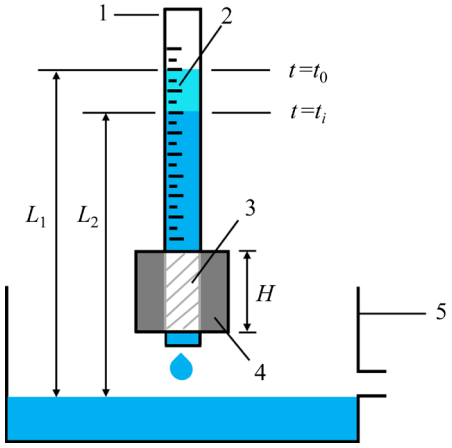

Fig. 3 Schematic diagram of permeability test device using falling head method: 1− Standpipe; 2−Water level difference; 3−Specimen; 4−Rubber ring; 5−Tank

3 Results and discussion

3.1 Results of FEA

Figure 4 shows the von Mises stress distribution and total deformation of four graded structures. As shown in Figs. 4(a)−(d), the stress is concentrated in the middle part of each cell which refers to the strut joints. This phenomenon is caused by the straight edges and sharp turns in structures, which is consistent with the strut-based structure BCC mentioned previously [38]. Although the stress was larger at the strut joint, overall the stress distribution was relatively uniform in the four graded structures, indicating that the graded structures in this study had excellent stress conduction ability. The results of the total deformation of four graded structures are similar to those of von Mises stress distribution (Figs. 4(e)−(h)), which exhibits uniform deformation.

Figure 5 exhibits the pressure distribution of four graded structures. It can be seen from Fig. 5 that the pressure distributions of four graded structures with different porosities are similar, namely, the pressure drops from the inlet to the outlet. The average pressure drop (ΔP) from the inlet to the outlet of P1, P2, P3, and P4 structures was 0.1832, 0.2421, 0.3279, and 0.4608 Pa, respectively. Based on ΔP, the permeability of four graded structures was calculated, and it decreased along with the porosity, which is consistent with the results of other literature [39,40]. The permeabilities of P1, P2, P3, and P4 structures are 54.6×10^{-9}, 41.3×10^{-9}, 30.5×10^{-9}, and 21.7×10^{-9} m^2, respectively, and all of them are close to the value of human bones.

The pore size of scaffolds is one of the important characteristics affecting new bone growth, and hence the pore sizes of graded structures were measured using the original 2D slice images. The distributions of pore sizes with different graded structures are shown in Fig. 6, where D_{50} was pore diameters of 50% at a cumulative frequency of pore sizes, and was usually used to represent the average

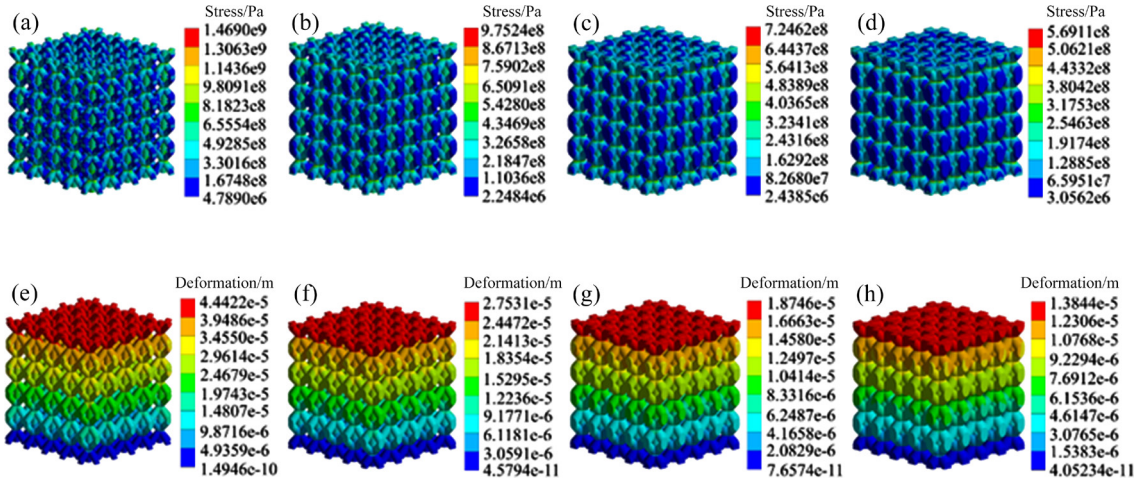

Fig. 4 von Mises stress distribution (a−d) and total deformation (e−h) of four graded lattice structures: (a, e) P1; (b, f) P2; (c, g) P3; (d, h) P4

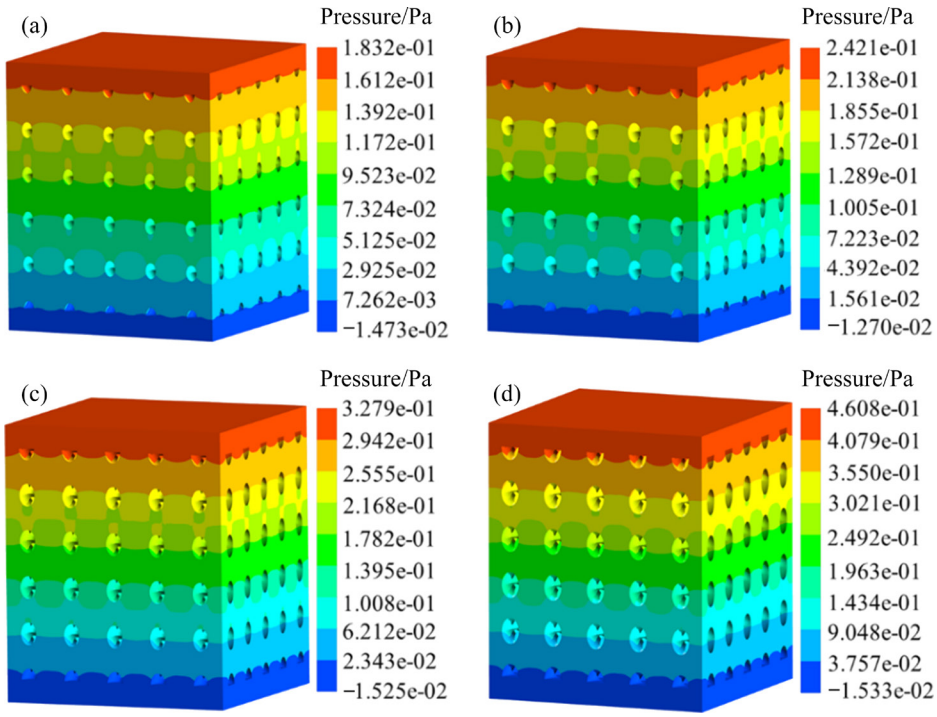

Fig. 5 Pressure distribution of four graded structures: (a) P1; (b) P2; (c) P3; (d) P4

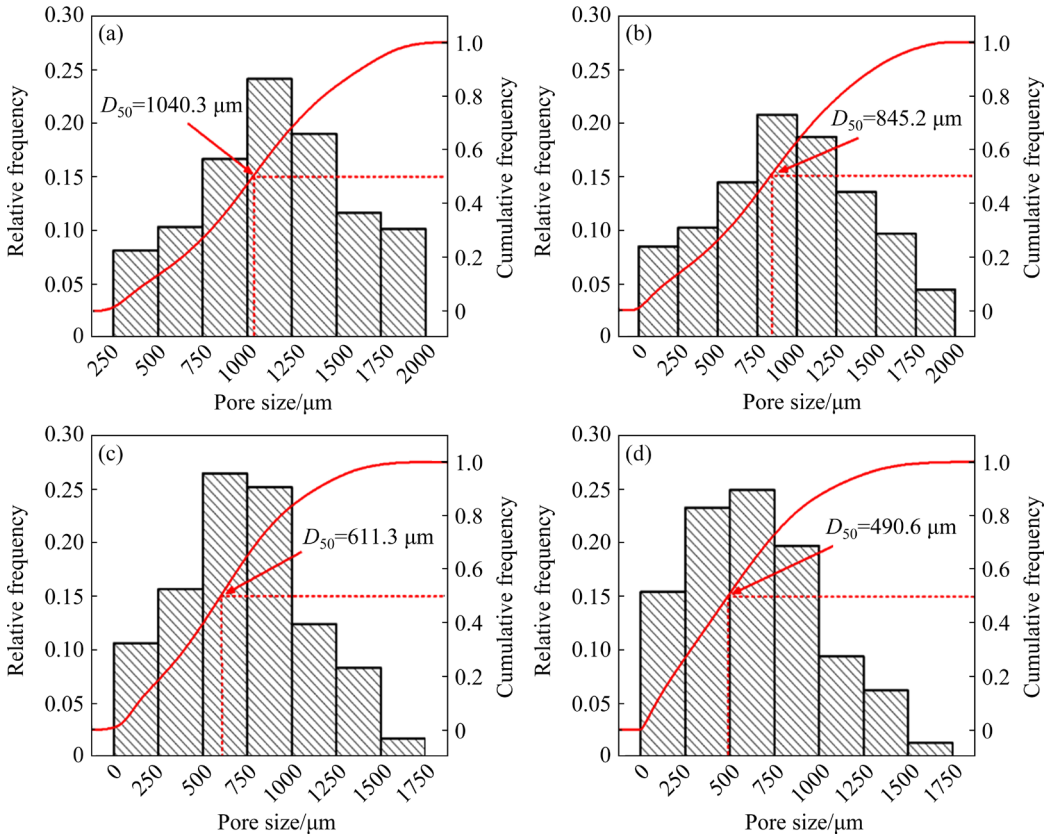

Fig. 6 Distribution of pore size of samples with different structures: (a) P1; (b) P2; (c) P3; (d) P4

pore size. It can be seen that the pore size distribution is in the ranges of 250−2000, 0−2000, 0−1750, and 0−1750 μm, respectively. With the average porosity increasing from 54.4% to 78.8% (P4 to P1), the average pore size increased from 490.6 to 1040.3 μm. It is commonly believed that the pore sizes of porous scaffolds in the range of 300−700 μm are beneficial for new bone

regeneration [24]. Thus, from the point of average pore size, the graded P3 and P4 structures are more suitable.

The permeability, the maximum von Mises stress, the maximum total deformation, and the pore size of four graded structures are summarized in Table 3. With the porosity increase (from P4 to P1), the permeability, maximum Von-Mises stress, and the maximum total deformation of four graded structures are in the range of $(21.7-54.6)\times10^{-9}$ m^2, (569.1−1469.0) MPa, and (0.0138−0.0444) mm, respectively. Among them, the permeability of P3 and P4 structures was close to that of human bones while the maximum von Mises stress was lower than the yield stress of dense CP-Ti material (830 MPa). Additionally, as analysed above, the average pore size of graded P3 and P4 structures favours bone regeneration. As a result, the graded structures P3 and P4 were selected and manufactured by SLM for the following study.

3.2 Manufacturability and microstructure

Figure 7 shows the designed CAD models, the fabricated samples, and corresponding SEM images of the fabricated samples after sand-blasting. It can be seen that the geometrical characteristics of as-built samples are consistent with CAD models without distinct defects. In order to evaluate the quality of SLM-fabricated samples further, the characteristics of designed CAD models and as-fabricated samples, including the strut radius, the porosity, and the pore size, are summarized in Table 4. The strut radius of as-built samples was found to be slightly larger than that of the CAD models while the porosity and pore size were marginally lower, but the deviation was low (<2%). This tiny deviation was attributed to a few residual partially melted powders which were not removed by simple mechanical methods, and the bumps (as yellow arrow shown in Fig. 7) were caused by stair-stepping effect. These results indicate that high-quality porous scaffolds can be obtained by SLM through simple post-processing methods such as sand-blasting and ultrasound cleaning.

Figure 8 presents the XRD patterns of graded CP-Ti scaffolds with P3 and P4 structures. The XRD patterns of different scaffolds were similar with only peaks of hexagonal-closed pack titanium (hcp-Ti) existed. However, compared with milled powders, there was a slight deviation in the

Table 3 FEA results of graded porous lattice structures

Model	Porosity/%	Permeability/ 10^{-9} m^2	Maximum von Mises stress/MPa	Maximum total deformation/mm	Average pore size/μm
P1	78.8	54.6±2.1	1469.0	0.0444	1040.3
P2	70.8	41.3±1.7	975.2	0.0275	845.2
P3	62.6	30.5±1.2	724.6	0.0187	611.3
P4	54.4	21.7±0.9	569.1	0.0138	490.6

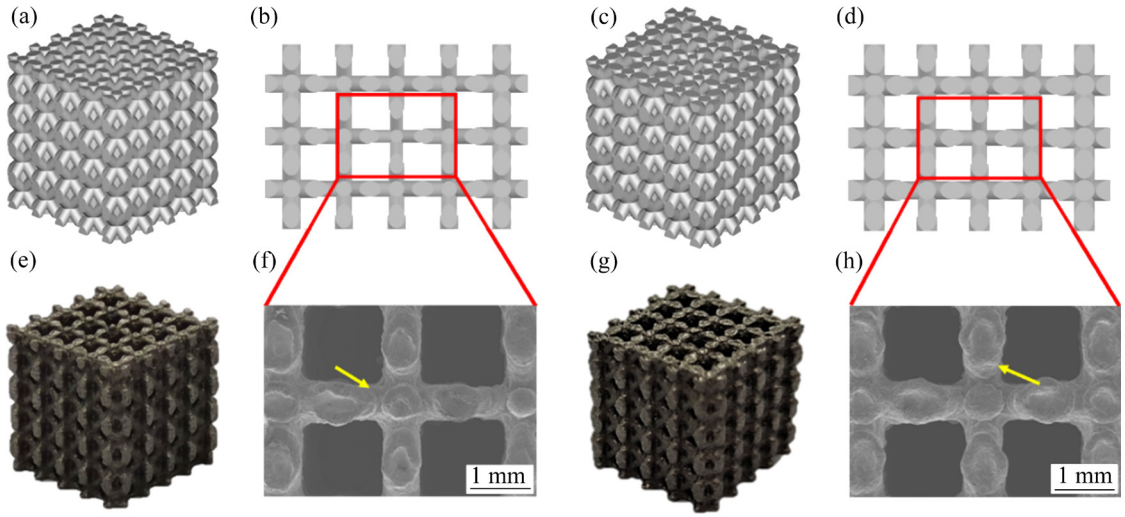

Fig. 7 Designed CAD models (a−d), SLM-fabricated samples (e, g), and corresponding SEM images (f, h) of SLM-fabricated samples after being sand-blasted: (a, b, e, f) P3; (c, d, g, h) P4

Table 4 Porous characteristics of as-built graded CP-Ti scaffolds with P3 and P4 structures in comparison to CAD models

Model	Design			As-built			
	Porosity/%	Strut radius/mm	Pore size/μm	Dry weighting porosity/%	CT porosity/%	Strut radius/mm	Pore size/μm
P3	62.6	0.25	611.3	61.7±0.3	61.9±0.2	0.252±0.002	601.6±0.8
		0.3				0.303±0.002	
		0.35				0.355±0.004	
P4	54.4	0.3	490.6	53.6±0.2	53.8±0.1	0.305±0.003	478.5±0.9
		0.35				0.355±0.003	
		0.4				0.406±0.004	

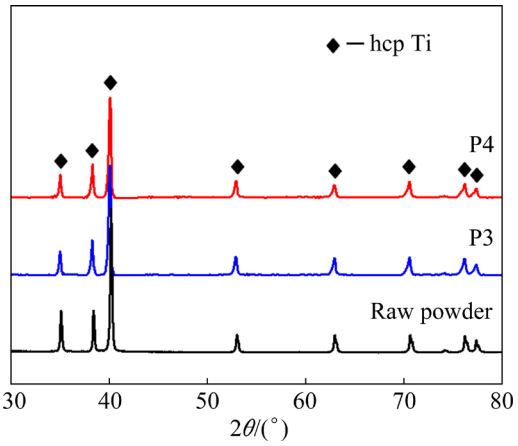

Fig. 8 XRD patterns of raw powder and as-built graded porous CP-Ti scaffolds with P3 and P4 structures

diffraction peaks of CP-Ti fabricated by SLM. The lattice parameters of as-built CP-Ti by SLM calculated by the XRD pattern were a=0.2949 nm and c=0.4703 nm, indicating that the phase was martensitic α' phase, which agreed with the previous studies [31]. The formation of α' phase can be attributed to the high rates of heating and cooling (10^3−10^8 K/s) during SLM processing which promotes the non-equilibrium phases transformation from β to α' [31].

Figures 9(a) and (b) show the microstructures of scaffolds with P3 and P4 structures. It can be seen that both scaffolds are completely dense without obvious pores. The microstructures of CP-Ti scaffolds with P3 and P4 structures were complete fine zigzag acicular martensitic α' phase without an obvious difference. Figures 9(c) and (d) show the TEM patterns of graded CP-Ti scaffold with P4 structure, and both brightfield images at low and high magnification show the fabricated sample consisted of acicular grains. The relevant selected area electron diffraction (SAED) image further indicated that the scaffold was an hcp-Ti structure (Fig. 9(d)), which agreed with the results of SEM and XRD patterns.

3.3 Permeability and mechanical properties

The permeability of scaffolds tested by the falling head method and CFD as well as natural bones are shown in Table 5. It can be seen that the permeability of graded CP-Ti scaffolds measured by the experiment increased with porosity, which was consistent with the simulation results and previous studies [37,39]. But the experimental values were lower than the results obtained by CFD. This was mainly due to the friction caused by the roughness of the as-built samples. A similar relationship between CFD analysis and experiment tests was also discovered by YU et al [15]. The experimental permeability of the CP-Ti scaffold with P4 structure was 18.62×10^{-9} m^2, which was in the range of permeability of natural bones ($(0.0268-20)\times10^{-9}$ m^2), meaning that CP-Ti with the P4 structure has good mass-transport properties to deliver oxygen and nutrition for bone tissue regrowth.

Figure 10 shows the engineering compressive stress−strain curves of graded CP-Ti scaffolds with P3 and P4 structures. Both two stress−strain curves began with a linear elastic stage. Then a plastic yield plateau stage occurred in both curves, and at this stage, the stress increased linearly with the strain slowly. After that, the stress−strain curve of the graded CP-Ti scaffold with P3 structure exhibited a fracture at about 35% strain. As for graded CP-Ti scaffold with P4 structure, the stress−strain curve showed a longer plastic yield plateau stage which was up to around 50% strain.

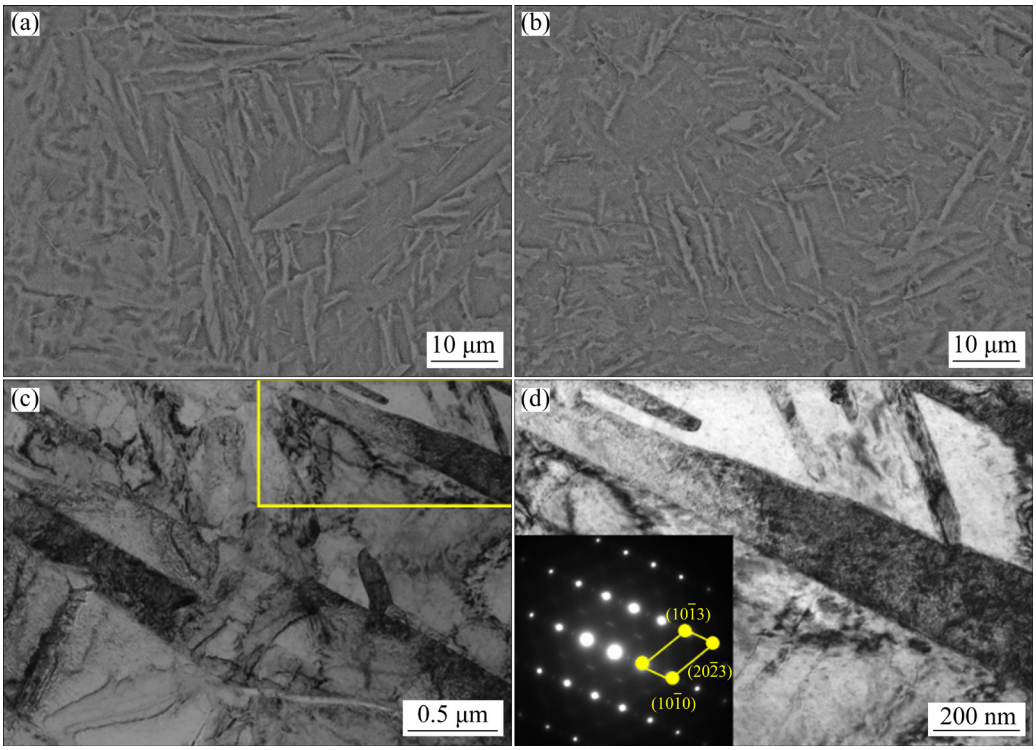

Fig. 9 SEM and TEM images of graded porous CP-Ti scaffolds: (a, b) SEM image of graded porous CP-Ti scaffolds with P3 and P4, respectively; (c) Brightfield image of graded porous CP-Ti scaffold with P4; (d) Brightfield image with higher magnification of graded porous CP-Ti scaffold with P4 (inserted SAED pattern)

Table 5 Permeability of graded lattice CP-Ti scaffolds with P3 and P4 structures measured by CFD and falling head method as well as natural bone

Scaffold	Porosity/ %	Simulated permeability/ 10^{-9} m^2	Measured permeability/ 10^{-9} m^2	Source
P3	61.9±0.3	30.5±1.2	27.1±0.8	This study
P4	53.8±0.2	21.7±0.9	18.6±0.6	This study
Natural bone	Up to 90	–	0.0268-20	[40]

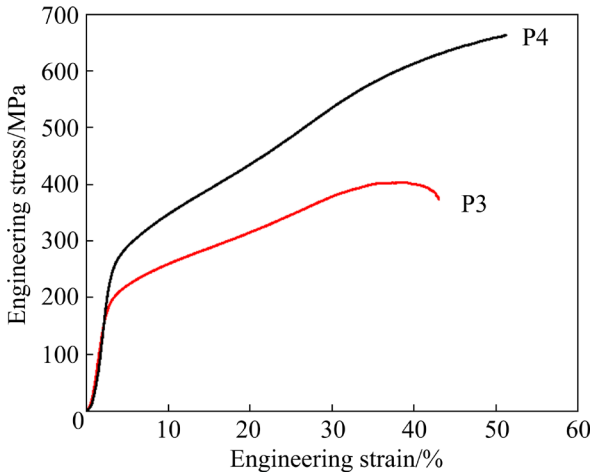

Fig. 10 Engineering compressive stress−strain curves of graded CP-Ti scaffolds with P3 and P4 structures

From the stress−strain curves, the yield strength and elastic modulus of the SLM-fabricated samples with P3 and P4 structures were obtained. Table 6 shows the mechanical properties of CP-Ti scaffolds with P3 and P4 structures in comparison to cortical bone, as well as CP-Ti or Ti64 with porous structures in the previous literature [15,26,37,41−43]. It can be found that the elastic moduli of as-built scaffolds in this study were 6.1 and 9.7 GPa, respectively, while the yield strengths were 185.3 and 250.8 MPa. Among them, the scaffold with the P4 structure exhibited a close elastic modulus to human natural bone, but the yield strength was 1.9 times that of cortical bone. Additionally, compared with the CP-Ti or Ti64

Table 6 Mechanical properties of graded porous CP-Ti scaffolds in this study in comparison with results from previous literature as well as cortical bone

Scaffold	Material	Porosity/%	Yield strength/MPa	Elastic modulus/GPa	Source
P3	CP-Ti	61.9±0.3	185.3±4.3	6.1±0.21	This study
P4	CP-Ti	53.8±0.2	250.8±4.8	9.7±0.25	This study
BCC	Ti−6Al−4V	65	153.0±8.6	4.7±0.1	[15]
P3	Ti−6Al−4V	48.4	156.1±20.3	9.01±0.35	[37]
Cellular	CP-Ti	37	113±0.3	13.1±0.3	[41]
C1 FGM	Ti−6Al−4V	65	113.0±2	4.3±0.2	[26]
Step-wise FGPB	Ti−6Al−4V	56.4	170.6±15.6	10.44±0.2	[37]
Dense-in	Ti−6Al−4V	62	114±8	3.9±0.8	[42]
Cortical bone	bone	5	131±20.7	10.1±2.4	[43]

porous scaffolds in literature at a similar porosity, the scaffold with the P4 structure shows a similar elastic modulus but higher yield strength. These results mean that the graded scaffold with the P4 structure not only can avoid stress shielding but also is strong enough to bear the loading force during implantation. As a result, excellent mechanical properties, appropriate permeability, and high porosity make graded CP-Ti scaffold with P4 structure a promising candidate for biomedical implant applications.

4 Conclusions

(1) Compared with P1 and P2 structures, P3 and P4 structures exhibit lower maximum Von-Mises stress, meaning that these two structures have higher mechanical properties. The simulated permeabilities of P3 and P4 structures are 30.5×10^{-9} and 21.7×10^{-9} m^2 respectively and close to that of the human bone.

(2) Compared with CAD models, the porosity and pore size of the SLMed samples decrease slightly while the strut radius increases mildly, but the deviation is in a reasonable range (<2%). All fabricated samples are dense without holes, demonstrating that the printing quality is high.

(3) The microstructure of fabricated scaffolds consists of acicular martensite. The elastic modulus of graded scaffolds with P4 structure is close to the natural bones while the compressive yield strength is 1.9 times that of natural bones. The permeability of scaffolds with P4 structure is 18.6×10^{-9} m^2, which is in the range of natural bones.

(4) Compatible elastic modulus, higher yield strength, appropriate permeability and high porosity make graded scaffolds with P4 structure a promising candidate for bone restorations, and therefore it can be considered for further study for using as orthopaedic implants.

Acknowledgments

This work was supported by the National Natural Science Foundation of China (Nos. 51922004, 51874037), State Key Lab of Advanced Metals and Materials, University of Science and Technology Beijing, China (Nos. 2019Z-14, 2020Z-04, 2021Z-03), Fundamental Research Funds for the Central Universities, China (Nos. FRF-TP-19005C1Z, 06500236), Interdisciplinary Research Project for Young Teachers of USTB, China (Fundamental Research Funds for the Central Universities, FRF-IDRY-20-023), Postdoctor Research Foundation of Shunde Graduate School of University of Science and Technology Beijing, China (No. 2022BH001), the China Postdoctoral Science Foundation (No. 2021M700377), and the Beijing Natural Science Foundation, China (No. 2212035). Chao-zong LIU and Maryam TAMADDON would like to acknowledge the support from the European Commission via the H2020 MSCA RISE BAMOS program (No. 734156), Innovate UK via Newton Fund (No. 102872), and Engineering and Physical Science Research Council (EPSRC) via DTP case programme (No. EP/T517793/1).

References

[1] YUAN Li, DING Song-lin, WEN Cui-e. Additive manufacturing technology for porous metal implant applications and triple minimal surface structures: A review [J]. Bioactive Materials, 2019, 4: 56−70.

[2] XU Wei, HOU Chen-jin, MAO Yu-xuan, YANG Lei, TAMADDON M, ZHANG Jian-liang, QU Xuan-hui, LIU Chao-zong, SU Bo, LU Xin. Characteristics of novel Ti−10Mo−*x*Cu alloy by powder metallurgy for potential biomedical implant applications [J]. Bioactive Materials, 2020, 5: 659−666.

[3] XU Wei, LU Xin, TIAN Jing-jing, HUANG Chao, CHEN Miao, YAN Yu, WANG Lu-ning, QU Xuan-hui, WEN Cui-e. Microstructure, wear resistance, and corrosion performance of Ti35Zr28Nb alloy fabricated by powder metallurgy for orthopedic applications [J]. Journal of Materials Science & Technology, 2020, 41: 191−198.

[4] LU Xin, ZHANG Da-wei, XU Wei, YU Ai-hua, ZHANG Jia-zhen, TAMADDON M, ZHANG Jian-liang, QU Xuan-hui, LIU Chao-zong, SU Bo. The effect of Cu content on corrosion, wear and tribocorrosion resistance of Ti−Mo−Cu alloy by powder metallurgy for load-bearing bone implants [J]. Corrosion Science, 2020, 177: 109007.

[5] SITI-NUR-HAZWANI M R, LIM L X, LOCKMAN Z, ZUHAILAWATI H. Fabrication of titanium-based alloys with bioactive surface oxide layer as biomedical implants: Opportunity and challenges [J]. Transactions of Nonferrous Metals Society of China, 2022, 32(1): 1−44.

[6] XU Wei, CHEN Miao, LU Xin, ZHANG Da-wei., SINGH H P, YU Jian-shu, PAN Yu, QU Xuan-hui, LIU Chao-zong. Effects of Mo content on corrosion and tribocorrosion behaviours of Ti−Mo orthopaedic alloys fabricated by powder metallurgy [J]. Corrosion Science, 2020, 168: 108557.

[7] HAN Li-ying, WANG Cun-shan. Microstructure and properties of $Ti_{64.51}Fe_{26.40}Zr_{5.86}Sn_{2.93}Y_{0.30}$ biomedical alloy fabricated by laser additive manufacturing [J]. Transactions of Nonferrous Metals Society of China, 2020, 30: 3274−3286.

[8] ATAEE A, LI Yun-cang, BRANDT M, WEN Cui-e. Ultrahigh-strength titanium gyroid scaffolds manufactured by selective laser melting (SLM) for bone implant applications [J]. Acta Materialia, 2018, 158: 354−368.

[9] IBRAHIM M K, SAUD S N, HAMZAH E, NAZIM E M. Role of Ag addition on microstructure, mechanical properties, corrosion behavior and biocompatibility of porous Ti−30at.%Ta shape memory alloys [J]. Journal of Central South University, 2020, 27(11): 3175−3187.

[10] ZADPOOR A A. Mechanical performance of additively manufactured meta-biomaterials [J]. Acta Biomaterialia, 2019, 85: 41−59.

[11] WANG Xiao-hua, LI Jin-shan, HU Rui, KOU Hong-chao. Mechanical properties and pore structure deformation behaviour of biomedical porous titanium [J]. Transactions of Nonferrous Metals Society of China, 2015, 25(5): 1543−1550.

[12] XU Wei, LIU Zhou, LU Xin, TIAN Jing-jing, CHEN Gang, LIU Bo-wen, LI Zhou, QU Xuan-hui, WEN Cui-e. Porous Ti-10Mo alloy fabricated by powder metallurgy for promoting bone regeneration [J]. Science China Materials, 2019, 62(7): 1053−1064.

[13] YANG Xin, ZHANG Zhao-yang, WANG Ben, MA Wen-jun, WANG Wan-lin, CHEN Wen-ge, KANG Ning-ning, LIU Shi-feng. Microstructure, mechanical properties and corrosion performance of selective laser melting Ti/GNPs composite with a porous structure [J]. Journal of Central South University, 2021, 28(8): 2257−2268.

[14] CHEN Zi-yu, YAN Xing-chen, YIN Shuo, LIU Liang-liang, LIU Xin, ZHAO Guo-rui, MA Wen-you, QI Wei-zhong, REN Zhong-ming, LIAO Han-lin, LIU Min, CAI Dao-zhang, FANG Hang. Influence of the pore size and porosity of selective laser melted Ti6Al4V ELI porous scaffold on cell proliferation, osteogenesis and bone ingrowth [J]. Materials Science & Engineering C, 2020, 106: 110289.

[15] YU Gui-sheng, LI Zhi-bin, LI Shuang-jian, ZHANG Qiang, HUA You-lu, LIU Hui, ZHAO Xue-yang, DHAIDHAI D T, LI Wei, WANG Xiao-jian. The select of internal architecture for porous Ti alloy scaffold: A compromise between mechanical properties and permeability [J]. Materials & Design, 2020, 192: 108754.

[16] GÓMEZ S, VLAD M D, LÓPEZ J, FERNÁNDEZ E. Design and properties of 3D scaffolds for bone tissue engineering [J]. Acta Biomaterialia, 2016, 42: 341−350.

[17] HAN Chang-jun, LI Yan, WANG Qian, WEN Shi-feng, WEI Qing-song, YAN Chun-ze, HAO Liang, LIU Jie, SHI Yu-sheng. Continuous functionally graded porous titanium scaffolds manufactured by selective laser melting for bone implants [J]. Journal of the Mechanical Behavior of Biomedical Materials, 2018, 80: 119−127.

[18] DERBY B. Printing and prototyping of tissues and scaffolds [J]. Science, 2012, 338: 921−926.

[19] XU Wei, LI Ming, WEN Cui-e, LV Shao-min, LIU Cheng-cheng, LU Xin, QU Xuan-hui. The mechanical properties and in vitro biocompatibility of PM-fabricated Ti−28Nb−35.4Zr alloy for orthopedic implant applications [J]. Materials, 2018, 11(4): 531−543.

[20] ZHAO Shuo, LI Shu-jun, WANG Shao-gang, HOU Wen-tao, LI Yi, ZHANG Lai-chang, HAO Yu-lin, YANG Rui, MISRA R D K, MURR L E. Compressive and fatigue behavior of functionally graded Ti−6Al−4V meshes fabricated by electron beam melting [J]. Acta Materialia, 2018, 150: 1−15.

[21] XU Wei, TIAN Jing-jing, LIU Zhou, LU Xin, HAYAT M D, YAN Yu, LI Z, QU Xuan-hui, WEN Cui-e. Novel porous Ti35Zr28Nb scaffolds fabricated by powder metallurgy with excellent osteointegration ability for bone-tissue engineering applications [J]. Materials Science & Engineering C, 2019, 105: 110015.

[22] BALLA V K, BODHAK S, BOSE S, BANDYOPADHYAY A. Porous tantalum structures for bone implants: Fabrication,

mechanical and in vitro biological properties [J]. Acta Biomaterialia, 2010, 6: 3349−3359.

[23] ZHENG Jing-pu, CHEN liang-jian, CHEN Dai-yuan, SHAO Chun-sheng, YI Man-fei, ZHANG Bo. Effects of pore size and porosity of surface-modified porous titanium implants on bone tissue ingrowth [J]. Transactions of Nonferrous Metals Society of China, 2019, 29(12): 2534−2545.

[24] BARBA D, ALABORT E, REED R C. Synthetic bone: Design by additive manufacturing [J]. Acta Biomaterialia, 2019, 97: 637−656.

[25] COSTA M M, DANTAS T A, BARTOLOMEU F, ALVES N, SILVA F S, MIRANDA G, TOPTAN F. Corrosion behaviour of PEEK or β-TCP-impregnated Ti6Al4V SLM structures targeting biomedical applications [J]. Transactions of Nonferrous Metals Society of China, 2019, 29(12): 2523−2533.

[26] CHOY S Y, SUN Chen-nan, LEONG K F, WEI Jun. Compressive properties of functionally graded lattice structures manufactured by selective laser melting [J]. Materials & Design, 2017, 131: 112−120.

[27] WU Yao-cheng, KUO Che-nan, WU T H, LIU Tai-you, CHEN Yi-wen, GUO X H, HUANG J C. Empirical rule for predicting mechanical properties of Ti−6Al−4V bone implants with radial-gradient porosity bionic structures [J]. Materials Today Communications, 2021, 27: 102346.

[28] FOUSOVÁ M, VOJTĚCH D, KUBÁSEK J, JABLONSKÁ E, FOJT J. Promising characteristics of gradient porosity Ti−6Al−4V alloy prepared by SLM process [J]. Journal of the Mechanical Behavior of Biomedical Materials, 2017, 69: 368−376.

[29] LIU Fei, MAO Zhong-fa, ZHANG Peng, ZHANG D Z, JIANG Jun-jie, MA Zhi-bo. Functionally graded porous scaffolds in multiple patterns: New design method, physical and mechanical properties [J]. Materials & Design, 2018, 160: 849−860.

[30] YANG Lei, MERTENS R, FERRUCCI M, YAN Chun-ze, SHI Yu-sheng, YANG Shou-feng. Continuous graded Gyroid cellular structures fabricated by selective laser melting: Design, manufacturing and mechanical properties [J]. Materials & Design, 2019, 162: 394−404.

[31] XU Wei, XIAO Shi-qi, LU Xin, CHEN Gang, LIU Cheng-cheng, QU Xuan-hui. Fabrication of commercial pure Ti by selective laser melting using hydride-dehydride titanium powders treated by ball milling [J]. Journal of Materials Science & Technology, 2019, 35: 322−327.

[32] XU Wei, YU Ai-hua, LU Xin, TAMADDON M, WANG Meng-di, ZHANG Jia-zhen, ZHANG Jian-liang, QU Xuan-hui, LIU Chao-zong, SU Bo. Design and performance evaluation of additively manufactured composite lattice structures of commercially pure Ti (CP-Ti) [J]. Bioactive Materials, 2021, 6: 1215−1222.

[33] SHI Jian-ping, YANG Ji-quan, LI Zong-an, ZHU Li-ya, LI Lan, WANG Xing-song. Design and fabrication of graduated porous Ti-based alloy implants for biomedical applications [J]. Journal of Alloys and Compounds, 2017, 728: 1043−1048.

[34] ZHANG Jian-feng, HU Yong-cheng, WANG Bao-cang, WANG Lei, WANG Hui, LI Yong, YAN Ming, LIU Hong-tao. 3D finite element analysis of the modular prosthesis with tooth mechanism of the femoral shaft [J]. Orthopaedic Surgery, 2020, 12(3): 946−956.

[35] VOSSENBERG P, HIGUERA G A, van STRATEN G, VAN-BLITTERSWIJK C A, VAN-BOXTEL A J B. Darcian permeability constant as indicator for shear stresses in regular scaffold systems for tissue engineering [J]. Biomechanics and Modeling in Mechanobiology, 2009, 8(6): 499−507.

[36] ISO 13314. Mechanical testing of metals−ductility testing−Compression test for porous and cellular metals [S]. 2011.

[37] ZHANG Xiang-yu, FANG Gang, LEEFLANG S, ZADPOOR A A, ZHOU Jie. Topological design, permeability and mechanical behavior of additively manufactured functionally graded porous metallic biomaterials [J]. Acta Biomaterialia, 2019, 84: 437−452.

[38] SMITH M B, GUAN Zhong-wei, CANTWELL W J. Finite element modelling of the compressive response of lattice structures manufactured using the selective laser melting technique [J]. International Journal of Mechanical Sciences, 2013, 67: 28−41.

[39] BOBBERT F S L, LIETAERT K, EFTEKHARI A A, POURAN B, AHMADI S M, WEINANS H, ZADPOOR A A. Additively manufactured metallic porous biomaterials based on minimal surfaces: A unique combination of topological, mechanical, and mass transport properties [J]. Acta Biomaterialia, 2017, 53: 572−584.

[40] MIHALCEA E, VERGARA-HERNÁNDEZ H J, JIMENEZ O, OLMOS L, CHÁVEZ J, ARTEAGA D. Design and characterization of Ti6Al4V/20CoCrMo−highly porous Ti6Al4V biomedical bilayer processed by powder metallurgy [J]. Transactions of Nonferrous Metals Society of China, 2021, 31(1): 178−192.

[41] ATTAR H, LÖBER L, FUNK A, CALIN M, ZHANG Lai-chang, PRASHANTH K G, SCUDINO S, ZHANG Yu-sheng, ECKERT J. Mechanical behavior of porous commercially pure Ti and Ti−TiB composite materials manufactured by selective laser melting [J]. Materials Science & Engineering A, 2015, 625: 350−356.

[42] ONAL E, FRITH J E, JURG M, WU Xin-hua, MOLOTNIKOV A. Mechanical properties and in vitro behavior of additively manufactured and functionally graded Ti6Al4V porous scaffolds [J]. Metals, 2018, 8(4): 200−221.

[43] WANG Xiao-jian, XU Shang-qing, ZHOU Shi-wei, XU Wei, LEARY M, CHOONG P, QIAN Ma, BRANDT M, XIE Yi-min. Topological design and additive manufacturing of porous metals for bone scaffolds and orthopaedic implants: A review [J]. Biomaterials, 2016, 83: 127−141.

基于选择性激光熔化技术的骨缺损修复用梯度多孔钛支架的研制与表征

于爱华[1]，徐 伟[1,2]，路 新[1,2,3]，Maryam TAMADDON[4]，刘博文[1]，
田世伟[5]，张 策[1]，Muhammad Arif MUGHAL[6]，张嘉振[1]，Chao-zong LIU[4]

1. 北京科技大学 工程技术研究院 高效轧制与智能制造国家工程研究中心，北京 100083；
2. 北京科技大学 顺德创新学院，佛山 528399；
3. 北京科技大学 新金属材料国家重点实验室 北京材料基因工程高精尖创新中心，北京 100083；
4. Institute of Orthopaedic & Musculoskeletal Science, University College London, Royal National Orthopaedic Hospital, Stanmore HA7 4LP, UK；
5. 北京科技大学 工程技术研究院 国家板带生产先进装备工程技术研究中心，北京 100083；
6. 北京科技大学 人工智能研究院，北京 100083

摘 要：为提高骨缺损修复的治疗效果，设计孔隙率为 78.8%、70.8%、62.6%和 54.4%的梯度多孔钛支架(分别表示为 P1，P2，P3 和 P4)，并通过选择性激光熔化技术进行制备。通过模拟和实验方法研究支架的成形性、显微组织、力学性能和渗透性能。模拟结果表明，4 种梯度结构的最大等效应力和渗透性分别在 569.1~1469.0 MPa 和 (21.7~54.6)×10^{-9} m^2 范围内，并且 P3 和 P4 具有更小的最大等效应力，表明 P3 和 P4 具有更高的强度。P3 和 P4 结构支架的显微组织为 α'马氏体，屈服强度和弹性模量分别为 185.3~250.8 MPa 和 6.1~9.7 GPa。相比于 P3 结构支架，P4 结构支架展现出更高的强度和与皮质骨更加匹配的弹性模量，并且其渗透性(18.6×10^{-9} m^2)在人体骨组织渗透性范围内。因此，具有 P4 结构支架有望被应用于骨科植入领域。

关键词：梯度多孔钛；骨植入体；选择性激光熔化；力学性能；渗透性

(Edited by Xiang-qun LI)